
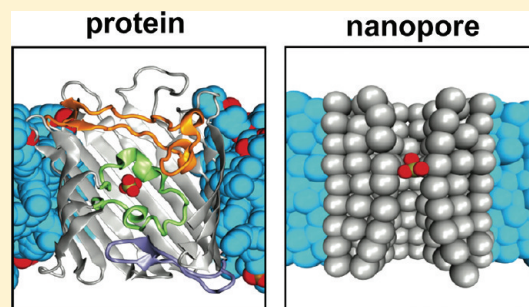


## Biomimetic Design of a Brush-Like Nanopore: Simulation Studies

Prapasiri Pongprayoon,<sup>†,‡</sup> Oliver Beckstein,<sup>†,§</sup> and Mark S. P. Sansom<sup>\*,†</sup><sup>†</sup>Department of Biochemistry, University of Oxford, South Parks Road, Oxford OX1 3QU, U.K.<sup>‡</sup>Department of Chemistry, Faculty of Science, Kasetsart University, P.O. Box 1011, Chatuchak, Bangkok 10903, Thailand Supporting Information

**ABSTRACT:** Combining a high degree of selectivity and nanoscale dimensions, biological pores are attractive potential components for nanotechnology devices and applications. Biomimetic design will facilitate production of stable synthetic nanopores with defined functionality. Bacterial porins offer a good source of possible templates for such nanopores as they form stable, selective pores in lipid bilayers. Molecular dynamics simulations have been used to design simple model nanopores with permeation free energy profiles that can be made to mimic a template protein, the OprP porin, which forms pores selective for anions. In particular, we explored the effects of varying the nature of pore-lining groups on free energy profiles for phosphate and chloride ions along the pore axis and the total charge of the permeation pathway of the pore. Cationic side chains lining the model nanopore are required to model the local detail of the OprP permeation landscape, whereas the total charge contributes to its magnitude. These studies indicate that a locally accurate biomimetic design has captured the essentials of the structure/function relationship of the parent protein.



## ■ INTRODUCTION

Nanopores in membranes have a number of possible applications, including as stochastic biosensors, as nanoreactors for single-molecule chemistry, as selective water pores for desalination, and as components of high throughput devices for biomedical diagnostics.<sup>1–5</sup> Such pores may be designed and synthesized de novo from nonbiological materials or may be obtained by re-engineering biological nanopores (e.g., channel and pore proteins from membranes). It is also possible to construct artificial biomimetic nanopores that reproduce some or all of the function of more complex biological systems, while offering the possibility of improved chemical and mechanical stability in technological applications.<sup>6–8</sup> For example, a recent study combined a gold-coated polycarbonate nanoporous membrane and natively unstructured proteins to generate artificial nanopores, which mimicked the transport properties of the nuclear pore complex.<sup>9</sup> Synthetic functional nanopores have also been based on the permeation properties of biological channels.<sup>10</sup>

Biomimetic design of synthetic nanopores offers the prospect of exploiting and extending the wide-ranging specificities of biological pores.<sup>11–13</sup> As exemplified by a recent study of K<sup>+</sup> vs Na<sup>+</sup> selectivity, computational methods can play a key role in aiding in the design of biomimetic pores.<sup>14</sup> Such a design process requires two key stages: (i) identification of suitable biological pore targets upon which to base a design and (ii) using computational methods to understand the quantitative origin of conductance and selectivity so that the function may be successfully transplanted to a nonbiological nanopore template.

Bacterial outer membrane proteins (and specifically porins) offer a good starting point for biomimetic design. As a consequence

of their  $\beta$ -barrel architecture, they are stable and readily mutable bionanopores,<sup>15,16</sup> offering a range of functionalities.<sup>17</sup> Porin selectivity seems to largely reside in the protein side chains rather than in the backbone as is the case in K channels<sup>18</sup> and in aquaporins.<sup>19</sup> Thus, the selectivity mechanisms of porins are more likely to be transplantable to synthetic nanopore templates.

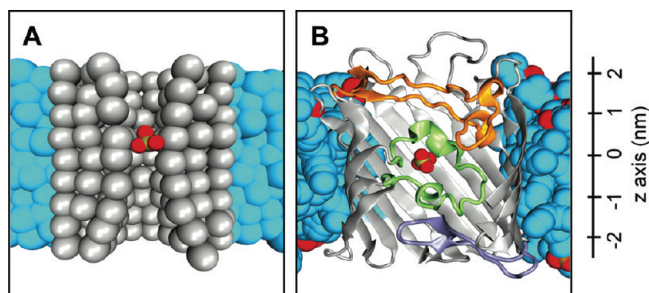
Computer simulations play a key role in the design of biomimetic pores. There is a long history of using molecular dynamics (MD) and related approaches to understand the selectivity and conductance properties of biological ion channels and pores (see e.g.<sup>20,21</sup>). In particular, calculations of the potential of mean force (PMF) of ions and other species as a function of their position within a selective protein pore have been used to establish the design principles of potassium channels<sup>22</sup> and of aquaporins.<sup>23</sup> More recently, a similar approach has been applied to a phosphate-selective porin, OprP.<sup>24</sup> MD simulation studies have also been used to explore simplified models of biomimetic nanopores, e.g., exploring the impact of geometry and pore-lining polarity on water and ion permeation.<sup>25–30</sup>

Here, we extend this latter approach to design a specific model nanopore, which is a functional mimic of the anion selective porin OprP (Figure 1). OprP conducts either chloride or phosphate anions but shows a ca. 600-fold higher affinity for phosphate.<sup>31</sup> In particular, we explore the effect of the nature and flexibility of pore-lining cationic groups on the PMF for phosphate and chloride ions along the pore axis. The resultant model

Received: July 15, 2011

Revised: November 18, 2011

Published: November 30, 2011

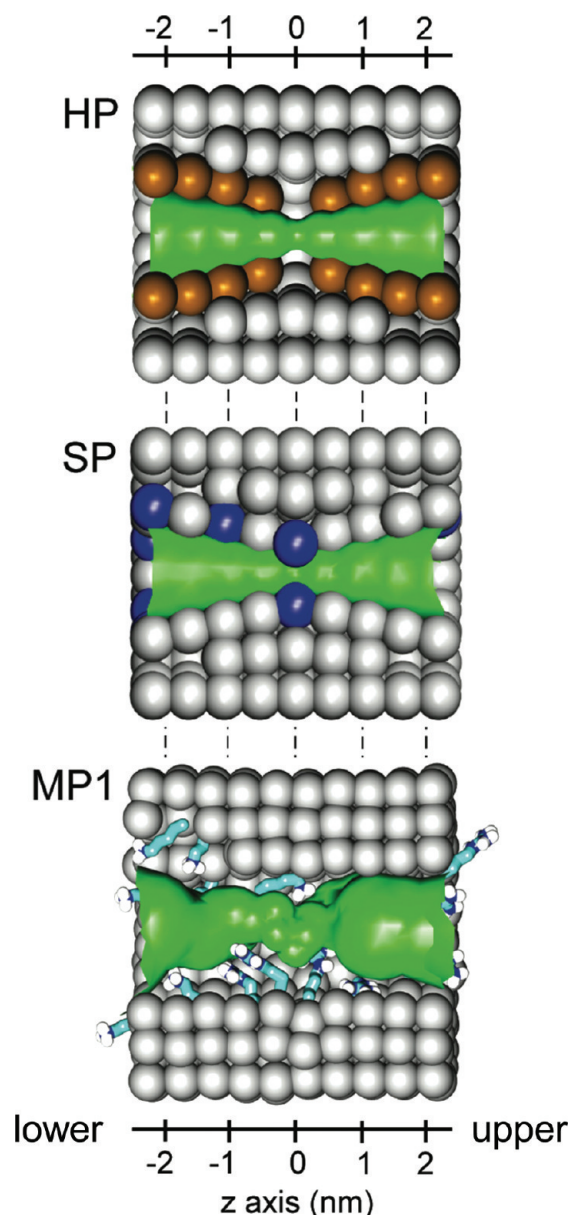


**Figure 1.** Representations of the biomimetic model nanopore and of the protein pore (OprP) on which this was based. (A) A model nanopore (HP, see Table 1) is shown in a cutaway space-filling format in gray, with the surrounding membrane mimic in cyan. A phosphate ion (red/yellow) is shown within the pore. Water molecules are omitted from both diagrams for clarity, and the approximate  $z$  axis is indicated. (B) The protein pore (OprP) shown in cutaway cartoon format with the barrel in gray, and three key loops in orange, green, and purple. The surrounding lipid bilayer is shown in a space-filling format as is a phosphate ion within the central pore.

is similar to OprP in its ion permeation properties suggesting that the biomimetic design has captured the essentials of the structure/function relationship of the parent protein.

## METHODS

**Model Construction.** Building upon earlier studies,<sup>26,27,32,33</sup> cylindrical model nanopores were constructed from cylindrical arrays of hydrophobic (methane-like) particles. Using this approach, the models were designed to mimic the dimensions and pore characteristics of OprP. Each model comprises concentric rings of methane particles with a van der Waals radius of 0.195 nm. A pore is composed of two mouth regions (radius  $\approx$  0.7 nm;  $1.75 \text{ nm} < \text{length} < 2.5 \text{ nm}$ ) and an inner pore region (radius  $\approx$  0.3 nm; length  $\approx$  0.5 nm). All methane-like particles were harmonically restrained to their initial position (with a force constant  $k_0 = 10\,000 \text{ kJ} \cdot \text{mol}^{-1} \cdot \text{nm}^{-2}$ ) in order to preserve the pore shape. Three models with different interior environments were constructed (Figure 2; Table 1). The hydrophobic pore (HP) provides an unmodified reference nanopore model with a pore radius profile similar to that of OprP. In the static charge (SP) and mobile charge (MP) models, the functionally important positive charges from the pore-lining of OprP (where they are formed by arginine and lysine side chains) were transplanted to the model pores. To construct a static charged pore (SP), 20 charges of +1 were assigned to given particles on an interior wall so as to match the spatial disposition of positively charged side chains inside the OprP pore. The mobile charged model (MP1) was created by attaching nine Arg and 11 Lys side chains extracted from the OprP crystal structure<sup>34</sup> onto the pore-lining surface, again to match the spatial distribution of these side chains in OprP. The end of each side chain toward the  $C_\alpha$  atom was capped with a methyl group, and its position was restrained by harmonic constraints with the same force constant  $k_0$  as the other particles forming the pore wall. (To study the effect of a reduced level of side chain flexibility, two further model pores, MP2 and MP3, were generated, which were similar to MP1 but with different lengths of pore-lining side chains; see Supporting Information, Figure S1.) On the basis of MP1, another model (named NP2) was prepared by adding a total charge of  $-12e$ . The charge was equally distributed over all 160 pore-facing



**Figure 2.** Three biomimetic nanopores: HP, a hydrophobic pore; SP, a pore with static pore-lining charges; and MP1, a pore with mobile (arginine-like and lysine-like) pore-lining charged groups. In each case, the background hydrophobic pore is shown in gray space-filling format, with the hydrophobic pore lining particles in bronze (HP), the cationic pore-lining particles in blue (SP), and the arginine-like and lysine-like groups in bonds format (MP1). For each pore, the pore-lining surface (as determined by HOLE<sup>35</sup>) is shown in green. The pore axis ( $z$ ) is indicated. A negative  $z$  value (the lower mouth of the pore) corresponds to the periplasmic mouth of the parent OprP porin.

methane-like particles ( $-0.075e$  per particle) in order to mimic the presence of a diffuse counter-charge background in the OprP pore. Pore radius profiles of all pore models were computed using HOLE.<sup>35</sup>

Each pore model was embedded in a simple membrane mimetic, formed from a slab of methane particles held on a cubic lattice (force constant  $3000 \text{ kJ} \cdot \text{mol}^{-1} \cdot \text{nm}^{-2}$ ). Water (SPC) molecules and counterions (consisting of 17  $\text{Cl}^-$  ions for SP and MP1 and 5  $\text{Cl}^-$  for NP2) were then added. Energy

**Table 1. Model Nanopores Used in This Study<sup>a</sup>**

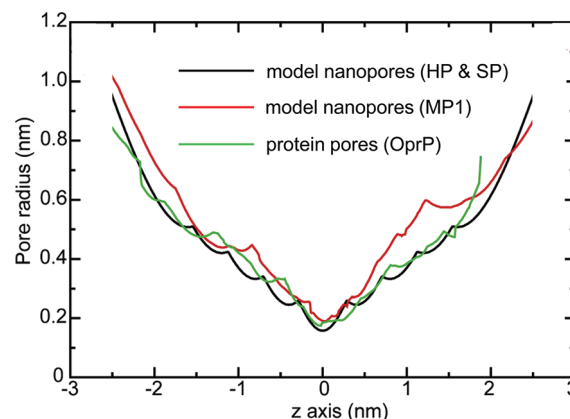
| model | description         | pore lining  |
|-------|---------------------|--|
| HP    | hydrophobic pore    | hydrophobic  |
| SP    | static charged pore | cationic: +20 charges positioned to OprP   |
| MP1   | mobile charged pore | cationic: 9 Arg and 11 Lys side chains   |
| MP2   | mobile charged pore | same as MP1, but side chains are truncated by 2 CH <sub>2</sub> groups   |
| MP3   | mobile charged pore | same as MP1, but side chains are truncated by 3 CH <sub>2</sub> groups   |
| NP2   | mobile charged pore | same as MP1, but an additional compensating background charge of $-12e$ was equally distributed over all pore-facing CH <sub>4</sub> -like particles |

<sup>a</sup> All model pores were designed to match the pore profile of OprP.

minimization (steepest descent algorithm) was run for 600 steps, followed by a 2 ns equilibration phase during which the pore framework was harmonically restrained with a force constant of  $k_0$ .

**MD Simulations.** All simulations were performed using GROMACS<sup>36</sup> version 3.3 ([www.gromacs.org](http://www.gromacs.org)) with the extended united atom GROMOS96 forcefield.<sup>36</sup> Long-range electrostatic interactions were treated using the particle mesh Ewald (PME) method<sup>37</sup> with a short-range cutoff of 1 nm, a Fourier spacing of 0.12 nm, and fourth-order spline interpolation. All simulations were performed in the NPT ensemble. The temperature of pore, membrane, solvent, and ions were coupled to a Berendsen thermostat<sup>38</sup> at 310 K with couple constant  $\tau_T = 0.1$  ps. The pressure was coupled semi-isotropically using the Berendsen algorithm at 1 bar with coupling constant  $\tau_P = 1$  ps. The time step for integration was 2 fs, and all bonds were constrained with the LINCS algorithm.<sup>39</sup> Data were analyzed using GROMACS and locally written code. Molecular graphic images were prepared using VMD.<sup>40</sup>

**Umbrella Sampling to Calculate Potential of Mean Force Profile.** Ion selectivity was explored by the calculation of potentials of mean force (PMFs), yielding free energy profiles for an anion as it is moved along the long ( $z$ ) axis of the pore. The 2 ns equilibrated pore systems were used as an initial structure for the umbrella sampling simulations. The 1D reaction pathway corresponds to the distance along the  $z$  axis between the center of mass of an anion (tribasic phosphate or chloride) and a pore model. It should be noted that this yields a single ion PMF for a pore that contains multiple ions, i.e., it provides an estimate of the free energy of the ion as it is moved along the pore axis, allowing all other degrees of freedom of the system (especially the locations of all other counterions and water molecules) to relax/equilibrate for each position of the selected ion. The range of interest ( $-3 \text{ nm} < z < 3 \text{ nm}$ ) was divided into 190 equidistant windows (each of width 0.05 nm). For each window simulation, an anion was placed into a pore at a center of an umbrella window, with the  $xy$  location of the ion determined by the pore radius profiles as calculated using HOLE.<sup>35</sup> Each window was initially equilibrated for 0.6 ns with an isotropic harmonic restraint of  $1000 \text{ kJ} \cdot \text{mol}^{-1} \cdot \text{nm}^{-2}$  on the anion. Umbrella sampling calculations were carried out by applying a harmonic biasing potential on the center of the anion relative to the center of mass of the pore; the force constant was  $1000 \text{ kJ} \cdot \text{mol}^{-1} \cdot \text{nm}^{-2}$  and acted only along  $z$ . Data were collected for 1 ns for HP and SP models and for 1.5 ns for MP1, and the last 700 ps of each run was used to construct the PMF. For NP2, each window was run for 3.5 ns, and the last 2.5 ns of each simulation was used to calculate the PMF. The unbiased PMF was computed with the weighted histogram analysis method (WHAM),<sup>41</sup> using Alan



**Figure 3.** Pore radius profiles (as determined using HOLE) for the model nanopores and for the parent protein OprP.

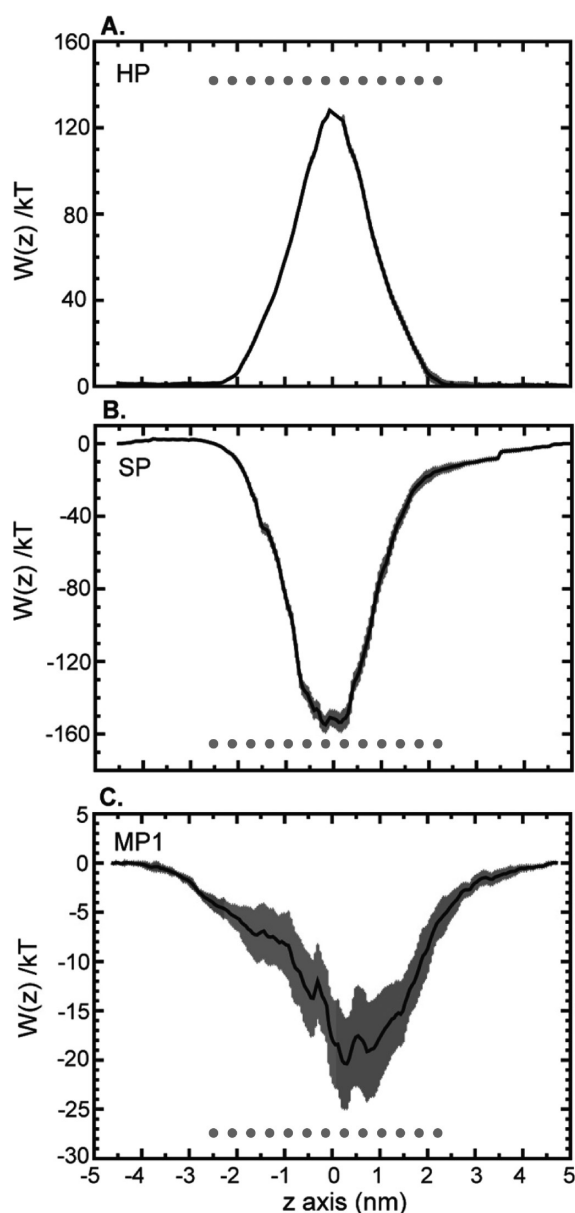
Grossfield's code (<http://membrane.urmc.rochester.edu/content/wham>). Errors were estimated from performing a block analysis<sup>42</sup> in the trajectory blocks of length 300 ps and averaging the block-PMFs. Dissociation constants of anion binding to the pore were computed from the PMFs using the method of Doudou et al.<sup>43</sup> as described previously for simulations of OprP.<sup>24</sup>

## RESULTS AND DISCUSSION

**Design Principles.** We wished to explore the influence of pore dimensions and pore-lining side chains on the ion permeation behavior through a model nanopore. The overall aim was to achieve a minimal design, which mimicked some key functional aspects of template protein, i.e., the OprP porin. As detailed above, we initially generated three simplified model nanopores with increasing levels of detail (Figure 2) to explore these effects. The HP pore mimics the shape of the OprP pore and presents a hydrophobic surface to the lumen. The SP model introduces the overall pattern and distribution of the positive charges characteristic of OprP in a static and coarse-grained fashion. The MP1 model increases the resolution of the model by replacing the static charges with side chain analogues of lysine and arginine residues and thus modeling the brush-like appearance of OprP.<sup>24</sup> Pore radius profiles (Figure 3) indicate that the model pores replicate the overall shape of the OprP pore with a central constriction of radius  $\sim 0.2$  nm and a pore length of  $\sim 5$  nm with pore mouths at either face of the membrane of radius  $\sim 0.7$  nm.

**Phosphate Energetics in the Pore.** A quantitative first view of the model nanopore properties is obtained from PMFs for a phosphate anion. The PMF corresponds to the free energy

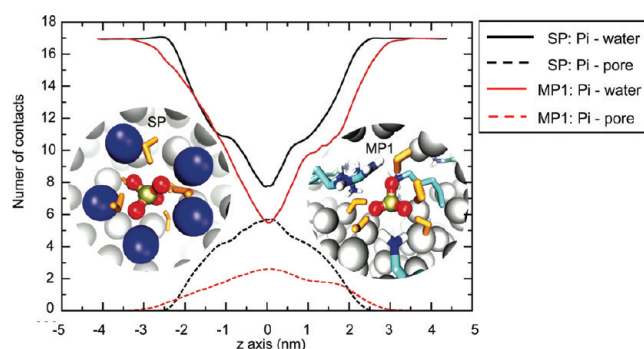




**Figure 4.** Phosphate PMF profiles for the (A) HP, (B) SP, and (C) MP1. Error bars (gray) are calculated from the block average. The horizontal dots indicate the extent of the nanopores along the pore ( $z$ ) axis.

profile for the anion as it is moved along a reaction coordinate, such as the pore ( $z$ ) axis. Phosphate translocation through the fully hydrophobic HP model is opposed by a barrier of  $\sim +120kT$  relative to the ion positions in the vestibules (Figure 4A). Barriers of comparable magnitude were also observed for  $\text{Na}^+$  ions in a study of uniformly narrow hydrophobic nanopores,<sup>27</sup> reflecting the energetic cost of ion desolvation without any compensatory interactions from the hydrophobic walls of the pore.

The pore with static charges lining the interior (SP) exhibits almost the opposite behavior, namely, a pronounced energy well of depth nearly  $-160kT$  (Figure 4B). Thus, as anticipated, a cationic pore exerts a strong attraction for anions. Such pronounced energy wells are likely to be a common feature of pores with a fixed high affinity binding site for a single ion.<sup>44</sup>

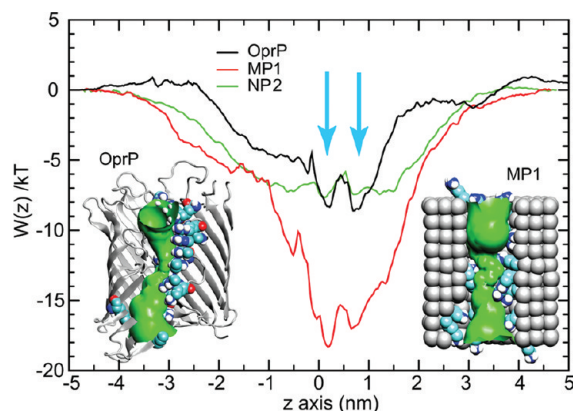


**Figure 5.** Average contact number of phosphate with water molecules (solid lines: black for SP, red for MP1) and with pore-lining particles (SP, black dashed line) or side chains (MP1, red dashed line) as a function of the phosphate ion position along the reaction coordinate ( $z$ ). All contacts are calculated using a cutoff of 0.5 nm. The inset figures show views down the pore of phosphate and its neighbors in the constriction site ( $z = 0$  nm) of SP and MP1 nanopores. Phosphate is represented in ball-and-stick format, waters in the first hydration shell in orange bonds format, and the cationic particles (SP) or side chains (MP1) in blue.

A more pore-like free energy profile is obtained in the MP1 model by mimicking the brush-like behavior of the pore lining of OprP (Figure 4C). The energy well is shallower with a depth of  $\sim -20kT$ . It is also broader, especially for the lower half (i.e.,  $z < 0$ ; see Figure 2) of the nanopore, which corresponds to the periplasmic opening and the selectivity filter of OprP.<sup>24</sup>

**Ion Solvation and Interaction with Pore Ligands.** The energetics of phosphate within the two charged types of model nanopore (SP and MP1) may be understood in more detail by considering the balance between pore/phosphate and water/phosphate interactions (Figure 5). As the phosphate anion enters the nanopore, it is partially dehydrated, with the number of water/phosphate contacts within a distance of 0.5 nm decreasing from  $\sim 17$  (in bulk water) to  $\sim 8$  (SP) or  $\sim 6$  (MP1) when at the central constriction. This dehydration is compensated for by the number of contacts with the positively charged groups lining the pore:  $\sim 6$  for SP and  $\sim 3$  for MP1 (Figure 5). Thus, for SP, the total number of contacts ( $\sim 14$ ) provides a nearly bulk-like coordination shell for phosphate at the constriction point. In contrast, within the narrowest region of the MP1 pore, phosphate loses  $\sim 11$  of water molecules from its hydration shell, but only  $\sim 3$  pore-lining side chains of MP1 are able to form contacts. Even though the number of contacts alone do not fully describe the energetics of solvation due to the different interactions between phosphate and the water dipoles versus phosphate and point charges on basic side chains, the analysis indicates the general trend of the phosphate anion to be highly spatially coordinated. Thus, the small total number of contacts with phosphate in MP1 ( $\sim 9$  compared to  $\sim 14$  total in SP) helps to explain the reduction in free energy well depth. It appears that the smearing of the cationic pore lining by the flexible side chains in MP1 provides more a pore-like energy profile.

We explored in a little more detail the effect of changing the degree of flexibility and size of the pore-lining side chains via removing either two or three  $-\text{CH}_2-$  groups from the arginine and lysine side chains lining the pore of MP1 to yield models MP2 or MP3, respectively (Supporting Information, Figure S1). Comparison of the phosphate PMFs for MP1, MP2 and MP3 (Supporting Information, Figure S2) revealed relatively small

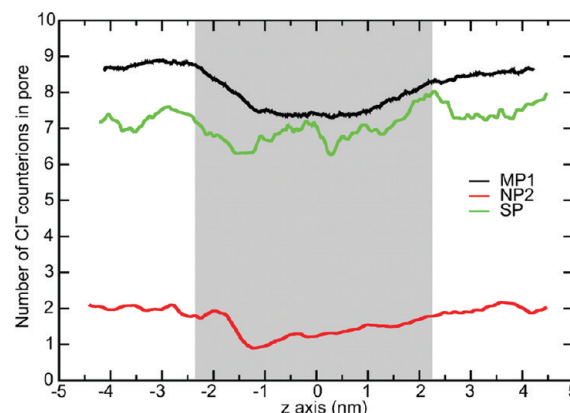


**Figure 6.** Comparison of the permeation free energy landscape of a phosphate ion through the template protein pore OprP (black), the MP1 model (red; flexible basic side chains), and the NP2 model (green; flexible basic side chains with negative background charge distributed over pore-lining). Error bars are omitted for clarity. The two vertical arrows indicate the approximate positions of the twin binding sites for phosphate at the center of the OprP pore. The inset figures compare the pore lining surfaces and side chains of MP1/NP2 and OprP.

differences in the overall depth of the energy well at the central constriction. However, the differences in side chain size and flexibility did result in changes in the PMF in the lysine-cluster region of the pore (i.e.,  $z = -2$  to  $0$  nm). Thus, the difference between the fixed charge (SP) and flexible charge models is reasonably robust to the details of the flexible side chains.

For reference, in the purely hydrophobic HP pore, the number of phosphate/water contacts is reduced to  $\sim 7$  water molecules at the constriction (data not shown), i.e., just over half of the hydration shell is displaced. In the absence of any compensating favorable electrostatic interaction with the pore, this explains the observed high free energy barrier for phosphate in the center of the HP pore. Analysis of the short-range electrostatic interactions between ion and environment supports the idea that electrostatic effects play a large role in determining the free energy landscape of permeation (see Supporting Information, Figure S3).

**Biomimetic vs Biological Nanopore.** It is useful to compare the properties of the MP1 model nanopore back to those of the template protein OprP (Figure 6; see ref 24 for details of PMF calculations on OprP). Replication of the charged architecture of OprP in MP1 produces a phosphate PMF profile similar in shape to that of OprP but with about 2-fold deeper wells. The deeper energy well found in MP1 is likely to be due to the presence of just the 20 cationic residues inside the pore, whereas OprP also contains 12 pore-lining anionic residues that can partially neutralize the positive charge. In part, this difference is compensated for by the presence of about 8  $\text{Cl}^-$  counterions within the MP1 pore (see Figure 7). Despite these differences, the two phosphate free energy profiles are remarkably similar in shape, including the fine structure of the double energy minimum at the narrowest central region of the two pores. In addition to this central interaction site, the lysine cluster at the lower mouth of MP1 (corresponding to the periplasmic mouth of OprP) results in the overall asymmetry of the phosphate PMF. Thus, the charged brush-like behavior of the cationic side chains, which is believed to play a key role in the permeation properties of OprP,<sup>24</sup> seems to have been successfully transplanted to the nonbiological model nanopore.

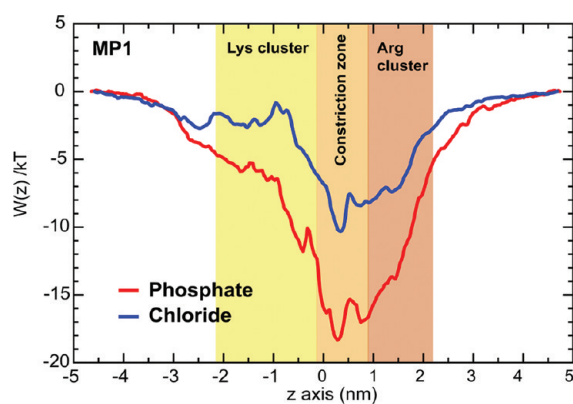


**Figure 7.** Number of  $\text{Cl}^-$  counterions within the model nanopores as a function of the phosphate position during the phosphate PMF umbrella sampling simulations. While the pore contained one phosphate anion, it also contained simultaneously up to nine chloride ions that freely adjusted their positions in response to the restrained phosphate.

The main remaining difference between the MP1 model and the OprP pore was the total charge in the permeation pathway of  $+20e$  versus  $+8e$ . We tested the hypothesis that the overall depth of the PMF is determined by the total charge of the pore by distributing a partially neutralizing charge of  $-12e$  (corresponding to the pore-lining acidic side chains in OprP) over all pore-lining particles. The resulting pore model NP2 had a total charge of  $+8e$  where basic side chains provided localized detail in a background of distributed negative charge, similar to the template biological pore. The phosphate PMF (Figure 6; also Supporting Information, Figure S4A) matches the OprP PMF reasonably well in both overall shape and magnitude. However, the distinct double well feature at the center of the pore has become somewhat less pronounced. The calculations, thus, establish the overall charge of the pore as an additional important design principle of ion-selective nanopores.

**Phosphate and Chloride.** A key property of the OprP porin is a difference in binding affinities between phosphate and chloride. Thus, OprP has a ca. 20-fold higher maximum conductance but a ca. 600-fold lower affinity for chloride than for phosphate.<sup>31,45</sup> This is manifested experimentally as a block of the chloride ionic current in the presence of low concentrations of phosphate. We, therefore, calculated a  $\text{Cl}^-$  PMF for MP1 to enable comparison between the properties of the two anions within the model nanopore. Side-by-side comparison of the  $\text{Cl}^-$  and phosphate PMFs for MP1 shows that phosphate is likely to bind more strongly in the constriction site than chloride, as the energy well is  $\sim 7kT$  deeper in the phosphate PMF (Figure 8). Furthermore, the lower vestibule, which mimics the Lys cluster of OprP, is attractive for phosphate but less so for  $\text{Cl}^-$ . These differences between the PMFs for the two anions, thus, mimic those seen for OprP. Calculating the dissociation constants for MP1 for the two anions<sup>43</sup> yields  $K_d$  values of  $0.45$  nM for phosphate and  $0.17$   $\mu\text{M}$  for  $\text{Cl}^-$  corresponding to  $\sim 400$ -fold stronger binding of phosphate than  $\text{Cl}^-$ , again mimicking the behavior of the template protein. Thus, in terms of anion selectivity the simulation results for MP1 reveal that the key functional aspects of a protein pore can be transferred to a nonbiological model by reproducing a small number of key aspects of the pore architecture.

The same method can be used to calculate the dissociation constant for phosphate for the NP2 model, yielding  $K_d = 34$   $\mu\text{M}$ .



**Figure 8.** Comparison of the PMFs for phosphate (red) and for chloride (black) for the MP1 model.

This agrees well with the experimental estimate of  $K_d = 90 \mu\text{M}$  for the template protein OprP.<sup>31</sup>

One should note that the phosphate PMF for MP1 is obtained in the presence of  $\text{Cl}^-$  counterions of which ca. 8 are located within the pore (Figure 7). In the NP2 model, the distributed background charge largely replaced these counterions and thus only 1 or 2  $\text{Cl}^-$  counterions entered the pore in addition to the phosphate (Supporting Information, Figure S4B). Thus, in both MP1 and NP2, the phosphate PMF is favorable in the presence of potentially competing  $\text{Cl}^-$  ions.

## CONCLUSIONS

We have designed a simple model nanopore based on an analysis of the structure/function relationships of a biological porin, OprP. The designed nanopore mimics the template protein in terms of providing a pore with comparable ion permeation free energy landscape and a degree of selectivity for phosphate over chloride. It, therefore, appears that the brush-like nature of the pore lining conferred by flexible cationic side chains is one way to obtain an anion-selective and permeable nanopore, combined with the total charge within the permeation pathway, which tunes the overall magnitude of the interactions with the ions. More generally, our results imply that a biomimetic design for a nanopore should capture, principally, the local features of the template protein in terms of pore geometry and electrostatics, while the more distant structural aspects of the nanopore may be somewhat less critical to the design. This general principle of design is relevant to modification of relatively featureless protein<sup>15</sup> or peptide<sup>46</sup> nanopores. We note that in the current study, we have focused on modification of side chains to achieve selectivity. If peptide backbone atoms play a role in channel selectivity (as is the case in, e.g., gramicidin A or KcsA), then a more nuanced approach to design may be required.<sup>14</sup>

In the current study, we have focused largely on the pore design and the use of PMFs to assess the strength (i.e., dissociation constants) of interactions with ions. In future studies, it will be important to focus more directly on the permeation process, per se, via, e.g., Brownian dynamics simulations suitably parametrized by MD simulations.<sup>47</sup> This will enable us to accurately estimate, e.g., single channel conductances, and directly explore, e.g., the block of ionic current by a competing ionic species.

The results described here complement those in recent studies of biomimetic nanopores, including, for example, a potassium-responsive nanopore based on quadruplex DNA;<sup>6</sup> a nanopore

designed to mimic the nuclear pore complex;<sup>9</sup> and a functional asymmetric nanopore based on asymmetric chemical modification of an hourglass-shaped nanochannel.<sup>7</sup> Overall, our results indicate that detailed computational analysis of the relationship between structure and function of models can reveal the general design principle for nanopores. Such studies may result in novel and technologically exploitable nanopores<sup>8</sup> selective for water-soluble organic analytes, such as drugs and related xenobiotics, for polymers<sup>3</sup> or for use in targeted cell killing.<sup>48</sup>

## ASSOCIATED CONTENT

**S Supporting Information.** Further information is provided on three aspects of the current study: (i) effects of flexibility of pore-lining groups; (ii) the change in energetic properties from SP to MP1; and (iii) counterions in the pore. This material is available free of charge via the Internet at <http://pubs.acs.org>.

## AUTHOR INFORMATION

### Corresponding Author

\*Tel: +44-1865-613306. E-mail: [mark.sansom@bioch.ox.ac.uk](mailto:mark.sansom@bioch.ox.ac.uk)

### Present Addresses

<sup>5</sup>Department of Physics, Arizona State University, Tempe, Arizona 85287–1504, United States.

## ACKNOWLEDGMENT

This work was supported by the Royal Thai government, the European Commission under the FP7 EDICT project (Grant No. 201924), the BBSRC, and the Wellcome Trust.

## REFERENCES

- (1) Bayley, H.; Cremer, P. S. *Nature* **2001**, *413*, 226.
- (2) Kasianowicz, J. J.; Robertson, J. W. F.; Chan, E. R.; Reiner, J. E.; Stanford, V. M. *Ann. Rev. Anal. Chem.* **2008**, *1*, 737.
- (3) Movileanu, L. *Trends Biotechnol.* **2009**, *27*, 333.
- (4) Corry, B. J. *Phys. Chem. B* **2008**, *112*, 1427.
- (5) Banerjee, A.; Mikhailova, E.; Cheley, S.; Gu, L. Q.; Montoya, M.; Nagaoka, Y.; Gouaux, E.; Bayley, H. *Proc. Natl. Acad. Sci. U.S.A.* **2010**, *107*, 8165.
- (6) Hou, X.; Guo, W.; Xia, F.; Nie, F.-Q.; Dong, H.; Tian, Y.; Wen, L.; Wang, L.; Cao, L.; Yang, Y.; et al. *J. Am. Chem. Soc.* **2009**, *131*, 7800.
- (7) Hou, X.; Yang, F.; Li, L.; Song, Y.; Jiang, L.; Zhu, D. *J. Am. Chem. Soc.* **2010**, *132*, 11736.
- (8) Hou, X.; Jiang, L. *ACS Nano* **2009**, *3*, 3339.
- (9) Jovanovic-Talman, T.; Tetenbaum-Novatt, J.; McKenney, A. S.; Zilman, A.; Peters, R.; Rout, M. P.; Chait, B. T. *Nature* **2009**, *457*, 1023.
- (10) Dehez, F.; Tarek, M.; Chipot, C. *J. Phys. Chem. B* **2007**, *111*, 10633.
- (11) Miedema, H.; Vroenenraets, M.; Wierenga, J.; Meijberg, W.; Robillard, G.; Eisenberg, B. *Nano Lett.* **2007**, *7*, 2886.
- (12) Titov, A. V.; Wang, B. Y.; Sint, K.; Kral, P. J. *Phys. Chem. B* **2010**, *114*, 1174.
- (13) Hou, X.; Guo, W.; Jiang, L. *Chem. Soc. Rev.* **2011**, *40*, 2385.
- (14) Gong, X.; Li, J.; Xu, K.; Wang, J.; Yang, H. *J. Am. Chem. Soc.* **2010**, *132*, 1873.
- (15) Chen, M.; Khalid, S.; Sansom, M. S. P.; Bayley, H. *Proc. Natl. Acad. Sci. U.S.A.* **2008**, *105*, 6272.
- (16) Reitz, S.; Cebi, M.; Reiss, P.; Studnik, G.; Linne, U.; Koert, U.; Essen, L. O. *Angew. Chem., Int. Ed.* **2009**, *48*, 4853.
- (17) Benz, R., Ed. *Bacterial and Eukaryotic Porins: Structure, Function, Mechanism*; Wiley-VCH Verlag GmbH&Co: Weinheim, Germany, 2004; p 360.



- (18) Zhou, Y.; Morais-Cabral, J. H.; Kaufman, A.; MacKinnon, R. *Nature* **2001**, *414*, 43.
- (19) Murata, K.; Mitsuoaka, K.; Hirai, T.; Walz, T.; Agre, P.; Heymann, J. B.; Engel, A.; Fujiyoshi, Y. *Nature* **2000**, *407*, 599.
- (20) Roux, B. *Curr. Opin. Struct. Biol.* **2002**, *12*, 182.
- (21) Roux, B.; Schulten, K. *Structure* **2004**, *12*, 1343.
- (22) Bernèche, S.; Roux, B. *Nature* **2001**, *414*, 73.
- (23) Hub, J. S.; de Groot, B. L. *Proc. Natl. Acad. Sci. U.S.A.* **2008**, *105*, 1198.
- (24) Pongprayoon, P.; Beckstein, O.; Wee, C. L.; Sansom, M. S. P. *Proc. Natl. Acad. Sci. U.S.A.* **2009**, *106*, 21614.
- (25) Hummer, G.; Rasaiah, J. C.; Noworyta, J. P. *Nature* **2001**, *414*, 188.
- (26) Beckstein, O.; Sansom, M. S. P. *Proc. Natl. Acad. Sci. U.S.A.* **2003**, *100*, 7063.
- (27) Beckstein, O.; Tai, K.; Sansom, M. S. P. *J. Am. Chem. Soc.* **2004**, *126*, 14694.
- (28) Cruz-Chu, E. R.; Aksimentiev, A.; Schulten, K. *J. Phys. Chem. C* **2009**, *113*, 1850.
- (29) Portella, G.; de Groot, B. L. *Biophys. J.* **2009**, *96*, 925.
- (30) Bond, P. J.; Guy, A. T.; Heron, A. J.; Bayley, H.; Khalid, S. *Biochemistry* **2011**, *50*, 3777.
- (31) Benz, R.; Egli, C.; Hancock, R. E. *Biochim. Biophys. Acta* **1993**, *1149*, 224.
- (32) Beckstein, O.; Biggin, P. C.; Sansom, M. S. P. *J. Phys. Chem. B* **2001**, *105*, 12902.
- (33) Beckstein, O.; Sansom, M. S. P. *Phys. Biol.* **2004**, *1*, 42.
- (34) Moraes, T. F.; Bains, M.; Hancock, P. E. W.; Strynadka, N. C. J. *Nat. Struct. Mol. Biol.* **2007**, *14*, 85.
- (35) Smart, O. S.; Neduvellil, J. G.; Wang, X.; Wallace, B. A.; Sansom, M. S. P. *J. Mol. Graph* **1996**, *14*, 354.
- (36) van der Spoel, D.; Lindahl, E.; Hess, B.; Groenhof, G.; Mark, A. E.; Berendsen, H. J. J. *Comput. Chem.* **2005**, *26*, 1701.
- (37) Darden, T.; York, D.; Pedersen, L. *J. Chem. Phys.* **1993**, *98*, 10089.
- (38) Berendsen, H. J. C.; Postma, J. P. M.; van Gunsteren, W. F.; DiNola, A.; Haak, J. R. *J. Chem. Phys.* **1984**, *81*, 3684.
- (39) Hess, B.; Bekker, H.; Berendsen, H. J. C.; Fraaije, J. G. E. M. *J. Comput. Chem.* **1997**, *18*, 1463.
- (40) Humphrey, W.; Dalke, A.; Schulten, K. *J. Mol. Graph* **1996**, *14*, 33.
- (41) Kumar, S.; Bouzida, D.; Swendsen, R. H.; Kollman, P. A.; Rosenberg, J. M. *J. Comput. Chem.* **1992**, *13*, 1011.
- (42) Flyvbjerg, H.; Petersen, H. G. *J. Chem. Phys.* **1989**, *91*, 461.
- (43) Doudou, S.; Neil, A.; Henchman, R. H. *J. Chem. Theor. Comput.* **2009**, *5*, 909.
- (44) Abad, E.; Reingruber, J.; Sansom, M. S. P. *J. Chem. Phys.* **2009**, *130*.
- (45) Benz, R.; Hancock, R. E. *J. Gen. Physiol.* **1987**, *89*, 275.
- (46) Ghadiri, M. R.; Granja, J. R.; Buehler, L. K. *Nature* **1994**, *369*, 301.
- (47) Vora, T.; Bisset, D.; Chung, S. H. *Biophys. J.* **2008**, *95*, 1600.
- (48) Majd, S.; Yusko, E. C.; Billeh, Y. N.; Macrae, M. X.; Yang, J.; Mayer, M. *Curr. Opin. Biotechnol.* **2010**, *21*, 439.